

Lyman- α forest/break²¹ absorption features through the U' band causes the model $U' - B'$ colours to move sharply redwards at $B' - I' \approx 0.7$ mag and the same effect is clearly seen in the data. The colours of 45 brighter, $B \approx 24$ mag galaxies with Keck redshifts are also shown in Fig. 3, and are also found to agree well with their predicted colours. (The equivalent $B' - R'$ versus $R' - I'$ graph is available: see Supplementary Information).

The above predictions show that, for the majority of faint galaxies, $U' - B' < 0$ is predicted to correspond to $z < 2$ galaxies and $U' - B' > 0$ corresponds to $z > 2$ galaxies. We find that the proportion of galaxies with $U' - B' > 0$ (including those undetected in U') rises to $47 \pm 7\%$ of the total at $27 \text{ mag} < B < 28 \text{ mag}$, indicating that the redshift distribution may peak at $z \approx 2$. This fraction is matched very well by both the $q_0 = 0.05$ model which predicts 47% with $U' - B' > 0$ at the same limit and the $q_0 = 0.5$, disappearing dwarf (dE) model which predicts 43%. We have also considered another $q_0 = 0.5$ model which assumes an extra population of low-redshift dwarf spirals (dSp) which evolve more slowly according to our standard exponential model for spiral luminosity evolution¹². Although this model also gives an improved fit to the counts, it predicts too few high-redshift ($U' - B' > 0$) galaxies (28%) for compatibility with the faint HST data.

These conclusions are confirmed by consideration of the $B' - R'$ versus $R' - I'$ colour-colour plot in Fig. 4. Figure 4a shows the predicted tracks of the galaxy types with redshift, as in Fig. 3. Also plotted are the galaxies with $U' - B' > 0$ and $R' < 27.5$ mag; these are expected to have $z > 2$ by the above arguments and it can be seen that their position on the $B' - R' : R' - I'$ tracks is entirely consistent with their lying in this redshift range. We regard this as crucial confirmation that our models are indicating consistent redshifts for galaxies in $U' - B'$ and $B' - R' : R' - I'$ independently. Figure 4b, c, d then show the HST data (dots) at $R' < 28$ mag compared to the predicted galaxy number contours for the open and closed models, based on the tracks shown in Fig. 4a. Both the $q_0 = 0.05$ and the $q_0 = 0.05$ dE model contours give a reasonable fit to the data which seem to peak at $B' - R' \approx 0.3$, $R' - I' \approx 0.3$, corresponding to $z \approx 2$ for all galaxy types. However, the $q_0 = 0.05$ dSp model contours peak away from this point at $B' - R' \approx 1$, $R' - I' \approx 1$ which corresponds to $z \approx 0.5$ for the dwarf spiral galaxies and we conclude that the galaxy redshift distribution in this model is skewed to too low redshifts to be compatible with the colour data. This does not mean that the above 'disappearing dwarf' model is unique in allowing a fit to be obtained with $q_0 = 0.5$; other possibilities such as merging models may also exist. However, it does suggest that, in any model, the star-forming phase has to be at $z \approx 2$ for consistency with the faint galaxy colours in the Hubble Deep Field. \square

Received 12 February; accepted 13 August 1996.

- Koo, D. C. & Kron, R. G. *Ann. Rev. Astron. Astrophys.* **30**, 613–652 (1992).
- Cowie, L. L. in *The Post-Recombination Universe* (eds Kaiser, N. & Lasenby, A.) 1–18 (Kluwer, Dordrecht, 1990).
- Williams, R. E. et al. *Astron. J.* (in the press).
- Metcalfe, N., Shanks, T., Fong, R. & Jones, L. R. *Mon. Not. R. Astron. Soc.* **249**, 481–497 (1991).
- Metcalfe, N., Shanks, T., Fong, R. & Roche, N. *Mon. Not. R. Astron. Soc.* **273**, 257–276 (1995).
- Cowie, L. L., Hu, E. M. & Songaila, A. *Nature* **377**, 603–605 (1995).
- Cowie, L. L., Songaila, A., Hu, E. M. & Cohen, J. G. *Astron. J.* (in the press).
- Shanks, T. in *The Galactic and Extragalactic Background Radiations* (eds Bowyer, S. & Leinert, C.) 269–281 (Kluwer, Dordrecht, 1990).
- Roche, N., Shanks, T., Metcalfe, N. & Fong, R. *Mon. Not. R. Astron. Soc.* **263**, 360–368 (1993).
- Glazebrook, K., Ellis, R. S., Santiago, B. & Griffiths, R. *Mon. Not. R. Astron. Soc.* **275**, L19–L22 (1995).
- Driver, S. P. et al. *Astrophys. J.* **449**, L23–L28 (1995).
- Bruzual, A. G. & Charlot, S. *Astrophys. J.* **405**, 538–553 (1993).
- Glazebrook, K. et al. *Mon. Not. R. Astron. Soc.* **273**, 157–168 (1995).
- Campos, A. & Shanks, T. *Mon. Not. R. Astron. Soc.* (submitted).
- Wang, B. *Astrophys. J.* **383**, L37–L40 (1991).
- Gronwall, C. & Koo, D. C. *Astrophys. J.* **440**, L1–L4 (1995).
- Lilly, S. J., Tresse, L., Hammer, F., Crampton, D. & Le Fevre, O. *Astrophys. J.* **455**, 108–124 (1995).
- Yoshii, Y. & Takahara, F. *Astrophys. J.* **326**, 1–18 (1988).
- Babul, A. & Rees, M. J. *Mon. Not. R. Astron. Soc.* **255**, 346–350 (1992).
- Lanzetta, K. M., Yahil, A. & Fernandez-Soto, A. *Nature* **381**, 759–763 (1996).
- Madau, P. *Astrophys. J.* **441**, 18–27 (1995).
- Small, I., Hogg, D. W., Yan, L. & Cohen, J. G. *Mon. Not. R. Astron. Soc.* (in the press).

- Driver, S. P., Philipps, S., Davies, J. I., Morgan, I. & Disney, M. J. *Mon. Not. R. Astron. Soc.* **268**, 393–404 (1994).
- Djorgovski, S. et al. *Astrophys. J.* **438**, L13–L16 (1995).
- Gardner, J. P., Cowie, L. L. & Wainscoat, R. J. *Astrophys. J.* **415**, L9–L12 (1993).
- Soifer, B. T. et al. *Astrophys. J.* **420**, L1–L4 (1994).
- McLeod, B. A., Bernstein, G. M., Rieke, M. J., Tollestrup, E. V. & Fazio, G. G. *Astrophys. J. Suppl. Ser.* **96**, 117–121 (1995).
- Glazebrook, K., Peacock, J. A., Collins, C. A. & Miller, L. *Mon. Not. R. Astron. Soc.* **266**, 65–91 (1995).
- Gardner, J. P., Sharples, R. M., Carrasco, B. E. & Frenk, C. S. *Mon. Not. R. Astron. Soc.* (submitted).

SUPPLEMENTARY INFORMATION. Available on Nature's World-Wide Web site <http://www.nature.com> or as paper copies from Mary Sheehan at the London editorial office of Nature.

ACKNOWLEDGEMENTS. We thank L. L. Cowie for allowing us to use results from the Keck 10-m redshift surveys in advance of publication, A. G. Bruzual for producing dwarf-dominated evolutionary models specially for this Letter, and the referees for helpful comments. We acknowledge the use of the Hubble Space Telescope Deep Field data. A.C. was supported by an EC Fellowship, and N.M. and J.P.G. by the UK PPARC.

CORRESPONDENCE should be addressed to T.S. (e-mail: Tom.Shanks@durham.ac.uk).

Entropic control of particle motion using passive surface microstructures

A. D. Dinsmore*, A. G. Yodh* & D. J. Pine†

* Department of Physics and Astronomy, University of Pennsylvania, 209 South 33 Street, Philadelphia, Pennsylvania 19104, USA

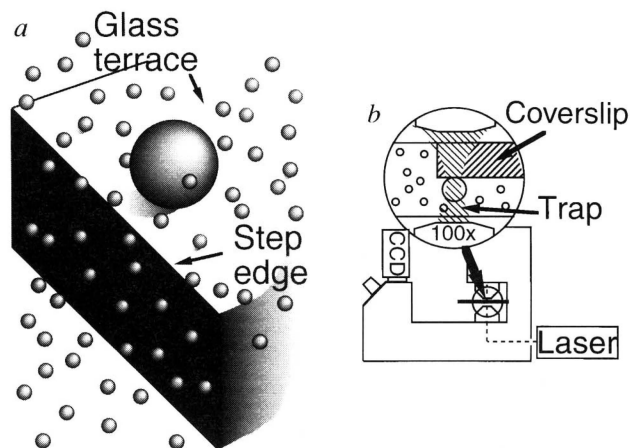
† Departments of Chemical Engineering and Materials, University of California, Santa Barbara, California 93106, USA

In a colloidal suspension containing particles of two different sizes, there is an attractive force between the larger particles. This attraction is due to the extra volume that becomes available to the smaller particles when the larger particles approach one another, thus increasing the entropy of the system. Entropic 'excluded-volume' effects of this type have been studied previously in colloids and emulsions, in the context of phase-separation phenomena in the bulk^{1–15} and at flat surfaces^{2,16}. Here we show how similar effects can be used to position the larger particles of a binary mixture on a substrate, or to move them in a predetermined way. Our experiments demonstrate the entropically driven repulsion of a colloidal sphere (in a suspension of smaller spheres) from the edge of a step; the magnitude of the entropic barrier felt by the sphere is approximately twice its mean thermal energy. These results indicate that passive structures etched into the walls of a container create localized entropic force fields which can trap, repel or induce the controlled drift of particles. Manipulation techniques based on these effects should be useful for making the highly ordered particle arrays required for structures with photonic band gaps^{17,18}, microelectronic mask materials¹⁹, and materials for clinical assays²⁰.

To demonstrate the entropic force-field idea in its barest form, we investigated the motions of hard spheres near the edge of a terrace (Fig. 1). We used an aqueous suspension of spherical polystyrene particles (Seradyn, Inc., Indianapolis) with diameters 0.460 μm and 0.083 μm and volume fractions 10^{-5} and 0.30, respectively. NaCl (0.01 M) was added to screen the electrostatic interactions over a distance of ~ 5 nm to obtain nearly ideal hard-core interactions¹⁶. As discussed below, the small spheres induce a 'depletion' attraction between the large spheres and the flat surface. Thus, a large sphere placed on the terrace diffused on its surface for several seconds (before escaping to the bulk). By following the two-dimensional trajectories of these spheres, we measured the forces acting on them near the step edge.

We quantify the effect of the step edge by measuring directly the Helmholtz free energy, F , of the system as a function of the position of the large sphere (Fig. 2a); we follow the analytical procedure given in ref. 21. Using video microscopy, we deter-

FIG. 1 a Drawing of a single large sphere near the edge of a terrace, representing the geometry of our experiment. The surrounding small spheres cause the large sphere to move in two dimensions on the surface and to be repelled from the step edge. The effect of gravity was negligible owing to the small particle sizes. b, Schematic diagram of the experimental apparatus. The (transparent) sample cell, $\sim 100\ \mu\text{m}$ thick, was placed in the microscope for viewing with a $100\times$ (numerical aperture = 1.3) oil-immersion objective with differential interference contrast (DIC). A polished-glass cover slip provided the smooth terrace and step edge inside the cell. Because ϕ_L (see text) was small, the large spheres were $10\text{--}20\ \mu\text{m}$ apart and did not interact with one another. A laser trap (1,053 nm wavelength radiation, 10 mW into the objective)^{28,29} was used to grab a single large sphere and place it on the terrace $0.56 \pm 0.06\ \mu\text{m}$ apart from the step edge. The laser trap was then turned off and the motions of the diffusing large sphere were followed using a CCD (charge-coupled-device) camera. We repeated the process to obtain $\sim 1,400$ events. Images 0.1 s apart were processed and the centre-of-mass sphere positions were measured with a precision of $0.04\ \mu\text{m}$. The total number of large spheres in view was 1,388 after 0.1 s but decreased by 33% over 4 s owing to escape of the spheres vertically from the flat surface into the bulk. In obtaining these data, we used several different $0.46\text{-}\mu\text{m}$ spheres and different sample cells, and always obtained similar results.



mined the probabilities, P_{ij} , that the large sphere jumped from the j th to the i th spatial bin during a time interval of length 0.1 s. We then computed the eigenvector of the matrix P with unit eigenvalue. The i th component of this eigenvector is proportional to $e^{-F_i/k_B T}$, where F_i is the Helmholtz free energy evaluated at the i th bin. The force on the large sphere points toward decreasing F with magnitude given by the gradient of F . To show the effect of the step edge on particle motions, we also present the probability distribution of the large-sphere positions at two times: 0.1 and 4.1 s after release (Fig. 2b, c).

Our results clearly exhibit free diffusion along the direction parallel to the step edge. The free energy was constant, indicating no net force (Fig. 2a, inset). Furthermore, as shown in Fig. 2b, the mean position, \bar{y} , remained zero and the probability distribution remained symmetric about the starting position (zero). The mean-square position, \bar{y}^2 , was proportional to time, as is characteristic of diffusion.

Perpendicular to the edge, however, there was a pronounced free-energy barrier approximately $2k_B T$ in magnitude, located at the step edge. As a large sphere moved towards the edge, the free

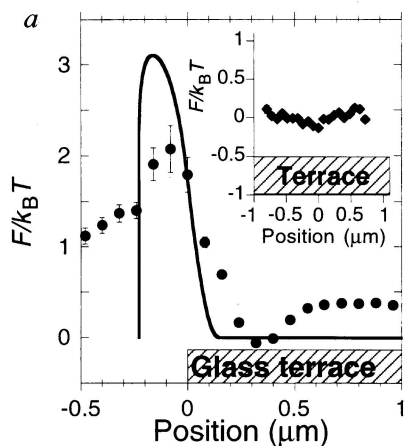
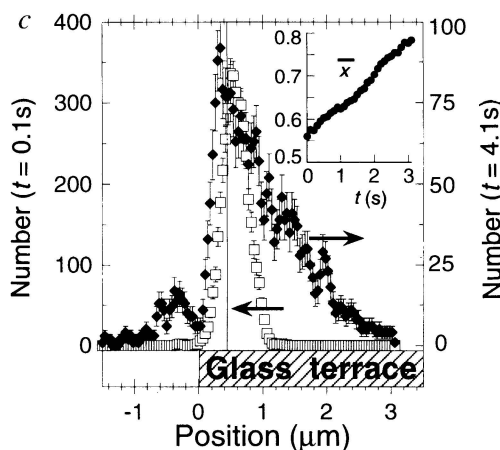
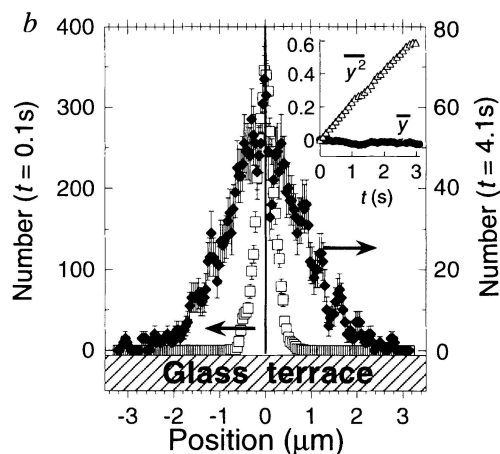


FIG. 2 a, Free energy of the system in units of the thermal energy, $F/(k_B T)$, as a function of the distance of a large sphere from a step edge located at zero. The filled circles represent measurements. The solid curve was calculated using the excluded-volume theory described in the text and treating the small spheres as an ideal gas with volume fraction 0.3. Although the ideal-gas approximation underestimates the pressure of a hard-sphere fluid, we use it because other quantitative effects (for example, non-uniform distribution of small spheres) are also ignored. Inset, plot of $F/(k_B T)$ versus large-sphere position parallel to the edge. There is no barrier. b, Measured probability distributions of a single large sphere in the direction parallel to the step edge at two different times after release from position zero. Empty squares (left axis), 0.1 s; filled diamonds (right axis), 4.1 s. The height of each data point gives the number of events in which the sphere was observed inside a $0.12\ \mu\text{m}$ -wide bin centred at that point. Inset: upper curve, measured mean-square position, \bar{y}^2 (μm^2), versus time, t (s), after release. Lower curve, mean position \bar{y} (μm). Error bars are smaller than the plot symbols. c, Measured probability distributions, at the same times after release as b, for motion perpendicular to the step edge. The vertical line indicates the starting position, $0.56\ \mu\text{m}$. Inset, plot of the mean position, \bar{x} (μm), versus t .



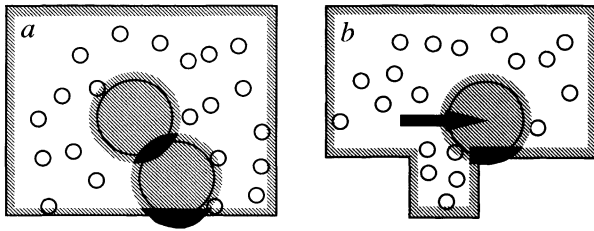


FIG. 3 Illustrations of the entropic interactions of hard spheres with surfaces. Owing to the hard-core repulsion, the small spheres' centres of mass are excluded from the hatched regions surrounding the large spheres and the walls. When the large spheres are separated from each other and from the walls, the volume accessible to the small spheres is the total volume of the box minus the hatched regions. *a*, When a large sphere touches another large sphere or a wall, the volume accessible to the small spheres (and, therefore, the entropy) increases by the volume of the 'excluded-volume overlap' region shown in black. This increase in entropy induces an attractive force between large spheres and walls. *b*, When a large sphere protrudes over a trench the excluded-volume overlap decreases, so that the sphere is repelled from the edge, as indicated by the arrow.

energy increased, equivalent to a force of $\sim 0.04 \times 10^{-12}$ N pushing the sphere back away from the edge. The probability distributions in Fig. 2c illustrate the effect of this barrier on particle motion. First, the distribution was asymmetric after 4.1 s, decreasing dramatically to the left of the edge because few of the spheres could 'escape' laterally across the edge of the terrace. Second, the peak of the probability distribution shifted from the starting point, towards the edge where the large spheres accumulated. If the large spheres simply diffused freely across the edge and disappeared from view, the probability-distribution peak would have shifted away from the edge. Third, the mean particle position, \bar{x} , increased (moved away from the edge) with time because the spheres were repelled from positions less than zero. We point out that the small dip in the free energy and the small peak in the late-time probability distribution near $-0.23 \mu\text{m}$ correspond to spheres that escaped across the barrier and were attracted to the vertical surface of the step. Last, the origin of the shallow free-energy minimum located $0.3 \mu\text{m}$ to the right of the edge is uncertain but may result from a non-uniformity in the small-sphere concentration induced by the step edge.

We stress that the lifetime of large spheres on the surface depends only on the concentration of small spheres. In a sample with small-sphere volume fraction reduced by 2 (to 0.15), the average lifetime of a large sphere on the surface was reduced by 3. Because other interactions (for example, electrostatic, van der Waals, or hydration forces) should not depend strongly on the small-sphere concentration, we concluded that they are much too weak to account for the forces here. (A measurement of the interaction between a polystyrene sphere and a glass wall is reported in ref. 22.)

To understand the origin of the repulsive force observed in the experiment, it is instructive to review the basic ideas behind entropically driven forces. A mixture of hard spheres maximizes its entropy by maximizing the volume accessible per particle. Although there exist only hard-core repulsions between pairs of particles, maximizing the entropy in the binary mixture can lead to an entropic attraction between the larger particles^{23,24} and between the particles and the walls^{16,25-27}. Figure 3a shows that, when a large sphere approaches another large sphere or the wall, the total volume available to the small spheres increases. This increases the total entropy of the mixture (decreases the Helmholtz free energy) by an amount proportional to the size of the 'excluded-volume overlap' region (represented in black) multiplied by the pressure of the small spheres. Specifically, moving a single large sphere from the bulk to the surface decreases the mixture's Helmholtz free energy by approximately $3(a_l/a_s)\phi_s k_B T$,

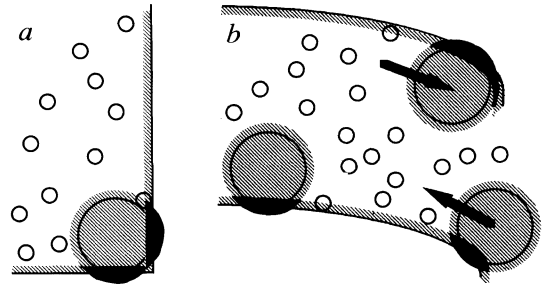


FIG. 4 Illustration of surface geometries that can trap the larger particles or induce drift. *a*, In a corner, the overlap volume (black region) is approximately twice as large as on a flat wall. Large spheres would tend to remain here for several seconds or minutes. Furthermore, the dense row of spheres in the corner could induce nucleation of highly ordered, three-dimensional crystals. *b*, Along a wall of changing curvature, the excluded-volume overlap changes with position. The larger sphere is driven along the wall in the direction of increasing overlap, as indicated by the arrows. Drift speeds up to approximately $0.1a_l$ per second may be obtained, where a_l is the diameter of the larger spheres.

where a_l (a_s) is the large- (small-) sphere diameter, $\phi_s = N_s \pi a_s^3 / (6V)$, and N_s is the number of small spheres in the sample of volume V (ref. 16). This free-energy gradient is equivalent to a force of $\sim 10^{-12}$ N pushing the large sphere towards the wall.

Consider a large sphere attracted by the depletion force to a surface into which a trench of width w has been cut (Fig. 3b). As the large sphere moves along the surface towards the trench, the amount of excluded-volume overlap changes. If the trench is wide enough to admit small spheres ($w > a_s$), then the excluded-volume overlap decreases (the free energy increases) as the large sphere protrudes over the edge of the trench; the trench acts like a barrier against the large sphere. The step edge of our experiment may be thought of as a trench with infinite w .

For comparison to our results, we have calculated the Helmholtz free energy, F , of the mixture as a function of the distance of a single $0.46 \mu\text{m}$ sphere from the edge, considering only the entropic excluded-volume effect. At the edge, there is a substantial free-energy barrier, the magnitude of which depends on the trajectory assumed for the large sphere. If we assume that it clings to the surface as it moves down around the corner of the step edge, the free energy increases to approximately $3k_B T$ at the edge, then returns to zero at $-0.23 \mu\text{m}$, where the sphere lies on the vertical surface (solid curve, Fig. 2a). By contrast, if we assume that the sphere moves at constant height, starting on the terrace far from the edge and moving horizontally past the edge, the free energy barrier exceeds $5k_B T$ (not shown). When the large sphere is slightly above the terrace, the magnitude of the barrier is reduced because the excluded-volume overlap is smaller. The fact that some of the particles in the experiment were slightly above the surface could explain why the measured barrier is less than $3k_B T$. The fact that the measured free energy does not return to zero to the left of the step at $-0.23 \mu\text{m}$ simply reflects our observation that some of the particles escaped into the bulk (where $F \approx 5k_B T$) while others went to the vertical surface of the step (where $F \equiv 0$).

Building on the effects demonstrated here, it is possible to devise structures that create potentially useful, localized and directional entropic force fields. A microscopic circular terrace could be used to trap a single large sphere which would be attracted vertically to the flat surface and constrained laterally by the step-edge barrier. An array of such terraces could be used to make the large spheres self-assemble in a chosen pattern. In Fig. 4a, we illustrate a large sphere attracted to an inside corner. In Fig. 4b, we show how net drift of large spheres over a large distance may be induced along a surface with changing curvature.

The strength and range of these entropic force fields can be controlled by varying ϕ_s , a_L and a_s , while the location and direction are determined by the substrate geometry. In practical systems, the effects are several $k_B T$ in magnitude and tens or hundreds of nanometres in range. □

Received 29 April; accepted 9 August 1996.

1. Pusey, P. N. & van Megen, W. *Nature* **320**, 340–342 (1986).
2. Dinsmore, A. D., Yodh, A. G. & Pine, D. J. *Phys. Rev. E* **52**, 4045–4057 (1995).
3. Bartlett, P., Ottewill, R. H. & Pusey, P. N. *Phys. Rev. Lett.* **68**, 3801–3804 (1992).
4. Sanyal, S., Easwar, N., Ramaswamy, S. & Sood, A. K. *Europhys. Lett.* **18**, 107–110 (1992).
5. van Duijnveldt, J. S., Heinen, A. W. & Lekkerkerker, H. N. W. *Europhys. Lett.* **21**, 369–374 (1993).
6. Imhof, A. & Dhont, J. K. G. *Phys. Rev. Lett.* **75**, 1662–1665 (1995).
7. Yasrebi, M., Shih, W. Y. & Aksay, I. A. *J. Colloid Interface Sci.* **142**, 357–368 (1991).
8. Steiner, U., Meller, A. & Stavans, J. *Phys. Rev. Lett.* **74**, 4750–4753 (1995).
9. Bibette, J., Roux, D. & Poulligny, B. *J. Phys. II Fr.* **2**, 401–424 (1992).
10. Calderon, F. L., Biais, J. & Bibette, J. *Colloids Surf. A* **74**, 303–309 (1993).
11. De Hek, H. A. & Vrij, A. *J. Colloid Interface Sci.* **84**, 409–422 (1981).
12. Calderon, F. L., Bibette, J. & Biais, J. *Europhys. Lett.* **23**, 653–659 (1993).
13. Ilett, S. M., Orrock, A., Poon, W. C. K. & Pusey, P. N. *Phys. Rev. E* **51**, 1344–1352 (1995).
14. Herzfeld, J. *Acc. Chem. Res.* **29**, 31–37 (1996).
15. Buitenhuis, J., Donselaar, L. N., Buining, P. A., Stroobants, A. & Lekkerkerker, H. N. W. *J. Colloid Interface Sci.* **175**, 46–56 (1995).
16. Kaplan, P. D., Rouke, J. L., Yodh, A. G. & Pine, D. J. *Phys. Rev. Lett.* **72**, 582–585 (1994).
17. Yablonovitch, E. *J. Opt. Soc. Am.* **10**, 283–295 (1993).
18. Joannopoulos, J. D., Meade, R. D. & Winn, J. N. *Photonic Crystals: Molding the Flow of Light* (Princeton Univ. Press, 1995).
19. Murray, C. A. & Grier, D. G. *Am. Sci.* **83**, 238–245 (1995).
20. Bangs, L. B. *J. Clin. Immunology* **13**, 127–131 (1990).
21. Crocker, J. C. & Grier, D. G. *Phys. Rev. Lett.* **73**, 352–355 (1994); *J. Colloid Interface Sci.* **179**, 298–310 (1996).
22. Prieve, D. C. & Frej, N. A. *Langmuir* **6**, 396–403 (1990).
23. Asakura, S. & Oosawa, F. *J. Polym. Sci.* **33**, 183–192 (1958).
24. Vrij, A. *Pure Appl. Chem.* **48**, 471–483 (1976).
25. Kaplan, P. D., Fauchaux, L. P. & Libchaber, A. *J. Phys. Rev. Lett.* **73**, 2793–2796 (1994).
26. Sober, D. L. & Walz, J. Y. *Langmuir* **11**, 2352–2356 (1995).
27. Milling, A. & Biggs, S. *J. Colloid Interface Sci.* **170**, 604–606 (1995).
28. Ashkin, A., Dziedzic, J. M., Bjorkholm, J. E. & Chu, S. *Opt. Lett.* **11**, 288–290 (1986).
29. Svoboda, K. & Block, S. M. *Annu. Rev. Biophys. Biomolec. Struct.* **23**, 247–285 (1994).

ACKNOWLEDGEMENTS. We thank T. C. Lubensky and P. D. Kaplan for useful conversations, and A. T. Johnson, Z. M. Yu, T. Heinzel and G. J. Dolan for their help in silicon processing. This work was supported by the US NSF and the PENN Materials Research Laboratory.

CORRESPONDENCE should be addressed to A.D.D. (e-mail: dinsmore@sol1.lrs.m.upenn.edu).

Direct U–Th dating of marine sediments from the two most recent interglacial periods

Niall C. Slowey*, Gideon M. Henderson† & William B. Curry‡

* Department of Oceanography, Texas A&M University, College Station, Texas 77843, USA

† Lamont-Doherty Earth Observatory, Columbia University, Palisades, New York 10964, USA

‡ Department of Geology and Geophysics, Woods Hole Oceanographic Institution, Woods Hole, Massachusetts 02543, USA

A KNOWLEDGE of the age of marine sediments is necessary to determine the timing of events and rates of processes in the marine realm, and the relationships among marine and other climatically sensitive records. The establishment of an accurate chronology for Pleistocene marine sediments beyond the range of radiocarbon dating (approximately the past 45 kyr) has therefore been a goal of palaeoceanographers for decades. Early attempts^{1,2} based on measurements of the radionuclides ²³⁰Th and ²³¹Pa were beset with problems, and subsequent studies focused on tying fluctuations in marine sediment oxygen-isotope records to events such as the formation of coral reef terraces and changes in the Earth's magnetic polarity^{3,4}, and tuning the resultant chronologies to the Earth's orbitally driven insolation variations^{5–8}. But

these chronologies (especially the age and duration of the last interglacial period) have been challenged by several studies^{9–12}, raising questions about the fundamental cause of Pleistocene climate fluctuations. Here we report the direct U–Th dating of aragonite-rich marine sediments from the Bahamas, and present an accurately dated marine oxygen-isotope record for the last two interglacials. We obtain dates of 120–127 kyr BP for the last interglacial and 189–190 kyr BP for the late stage 7 interglacial. These dates are in accord with the general theory of orbitally forced climate fluctuations and demonstrate the potential of our direct-dating approach for developing an absolute chronology for the Pleistocene marine oxygen-isotope record.

Algae and inorganic processes on the shallow edges and tops of Little Bahama Bank produce fine-grained aragonite with uranium concentrations far in excess of those found in foraminifera^{13–15} and which equal or exceed those of corals^{16,17}. Tides and storms cause this aragonite to become suspended in the water and transport it off the bank, whereupon it settles to the sea floor together with the normal rain of pelagic material¹⁸. Subaerial exposure of the banktop restricts aragonite production to the edge of the bank during sea-level lowstands, but the banktop sheds large quantities of material when flooded during interglacial highstands (sea level <15 m below present). Consequently, slope sediments possess expanded interglacial sections^{19–23} of U-rich marine sediments²⁴. They contain little terrigenous material, so detrital U and Th contents are small, and the shallow water depths mean that concentrations of Th scavenged from the water column are low. As these sediments have always been bathed in sea water they have not experienced diagenesis associated with exposure to meteoric water. The presence of typical marine microfossils and high primary U concentrations, coupled with low concentrations of detrital and scavenged Th, make interglacial Bahamian slope sediments ideal for direct U–Th dating of marine $\delta^{18}\text{O}$ record.

We sampled two wide-diameter piston cores (152JPC and 149JPC) from the southwestern slope of the Little Bahama Bank to test this approach (Table 1, Fig. 1). The cores were collected from the crests of ridges which extend down the slope, in order to isolate the sediment from possible disturbance by down-slope processes. In 152JPC, downcore variations of $\delta^{18}\text{O}$ and carbonate mineralogy indicate that sediments from the Holocene epoch and the last glaciation are not present. They slumped away

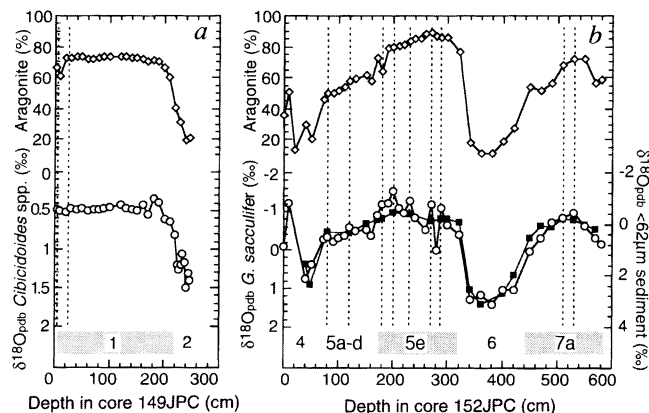


FIG. 1 The bulk-sediment aragonite percentage (diamonds), foraminiferal $\delta^{18}\text{O}$ (circles), and $<62\text{-}\mu\text{m}$ sediment fraction $\delta^{18}\text{O}$ records (filled squares) of core 149JPC (refs 23, 25; a) and core 152JPC (b). Vertical dashed lines indicate stratigraphic positions where samples were taken for radiocarbon and U–Th dating. Aragonite content was measured by X-ray diffraction. Foraminiferal $\delta^{18}\text{O}$ values are averages of two or more replicate analyses; $<62\text{-}\mu\text{m}$ sediment $\delta^{18}\text{O}$ values are typically single analyses (analytical uncertainty of any individual $\delta^{18}\text{O}$ analysis is 0.08‰). Marine $\delta^{18}\text{O}$ stages, as determined from the foraminiferal $\delta^{18}\text{O}$ stratigraphies, are shown by the shaded bars.